JGR Atmospheres

RESEARCH ARTICLE
10.1029/2018JD029205

Antarctic Ice Cloud Identification and Properties Using Downwelling Spectral Radiance From 100 to 1,400 cm^{-1}

Tiziano Maestri[1], Carlo Arosio[2], Rolando Rizzi[1], Luca Palchetti[3], Giovanni Bianchini[3], and Massimo Del Guasta[3]

[1]DIFA, Department of Physics and Astronomy, University of Bologna, Bologna, Italy, [2]IUP—Institute of Environmental Physics, University of Bremen, Bremen, Germany, [3]National Institute of Optics, INO at National Research Council, Sesto Fiorentino, Italy

Key Points:
- Spectral radiance measurements in the far infrared are used for cloud identification/classification
- Cloud properties are retrieved

Correspondence to:
T. Maestri,
tiziano.maestri@unibo.it

Citation:
Maestri, T., Arosio, C., Rizzi, R., Palchetti, L., Bianchini, G., & Del Guasta, M. (2019). Antarctic ice cloud identification and properties using downwelling spectral radiance from 100 to 1,400 cm^{-1}. *Journal of Geophysical Research: Atmospheres*, *124*, 4761–4781. https://doi.org/10.1029/2018JD029205

Received 20 JUN 2018
Accepted 5 APR 2019
Accepted article online 16 APR 2019
Published online 29 APR 2019

Author Contributions

Conceptualization: Tiziano Maestri, Carlo Arosio, Rolando Rizzi
Data curation: Luca Palchetti, Giovanni Bianchini, Massimo Del Guasta
Funding Acquisition: Tiziano Maestri, Rolando Rizzi
Methodology: Tiziano Maestri
Software: Tiziano Maestri
Validation: Tiziano Maestri
Writing - Original Draft: Tiziano Maestri
Formal Analysis: Tiziano Maestri
Investigation: Tiziano Maestri
Resources: Tiziano Maestri, Luca Palchetti
Supervision: Carlo Arosio, Rolando Rizzi
Visualization: Tiziano Maestri
Writing - review & editing: Tiziano Maestri, Carlo Arosio, Rolando Rizzi, Luca Palchetti

Abstract One year (2013) of high spectral resolution measurements of downwelling radiance in the 100–1,400 cm^{-1} range, taken by the Fourier Transform Spectrometer REFIR-PAD at the research station Concordia (Antarctic Plateau), is analyzed. Optically thin ice clouds are identified by means of a new identification/classification tool based on a Support Vector Machine algorithm. The use of transparent microwindow channels in the Far InfraRed (FIR) spectral region (100–667 cm^{-1}) is shown to be of great importance in the identification and classification of cloud type. In particular, the channels between 380 and 575 cm^{-1} are key channels for the clear/cloud and phase identification due to their sensitivity to cloud properties; in addition, FIR channels down to 238 cm^{-1} are exploited for the selection of precipitating or nonprecipitating cases because of their sensitivity also to water vapor content. A subset of 26 cases of nonprecipitating ice clouds is selected based on the presence of colocated LIDAR and radiosonde data. REFIR-PAD channel in the 800–1,000 cm^{-1} are used to derived optical and microphysical properties for four different assumptions concerning the crystal habits. Results, showing a correlation between cloud base temperature, optical depth, and particle size distribution effective dimensions, are compared with what found in literature. Based on the retrievals, forward simulations are also run over the whole sensor spectral interval, and results are compared to data. The simulation-data residuals in the FIR are evaluated for selected "window" channels and analyzed in relation to crystal's habit assumption, cloud retrieved features, and atmospheric water vapor content.

1. Introduction

The Far InfraRed (FIR) usually marks out the spectral region ranging from 667 cm^{-1} (approximately the center of the ν_2 vibrational band of the CO_2 at a wavelength 15 μm) to 100 cm^{-1} (equivalent to a wavelength of 100 μm). Radiative transfer in this spectral region is of great importance for climate and energy balance studies because it accounts for a large fraction of the Earth's outgoing energy flux and involves many key processes such as water vapor and clouds feedbacks. Despite its scientific importance, until the end of the last century, the FIR has represented a frontier in atmospheric research. Initially, there was a general interest among the scientific community, but atmospheric observations at these wavelengths were prevented by technological difficulties. New solutions were soon explored in order to achieve the desired radiometric range, resolution, and accuracy. In the paper by Harries et al. (2008), the reader can find a review of the main physical processes occurring at the FIR wavelengths and the main spectral sensors developed so far. In 2016, National Aeronautic and Space Administration (NASA) launched the Radiometer Assessment using Vertically Aligned Nanotubes CubeSat mission (Swartz et al., 2016) with the aim to verify the accuracy of calibration sources covering also the FIR spectral region. Recently, NASA has also selected the Polar Radiant Energy in the FIR Experiment (https://science.jpl.nasa.gov/projects/PREFIRE/), which has the objective to measure the top-of-atmosphere spectral radiance from 222 to 2,000 cm^{-1}.

Recently, the FIR has gained importance also for the remote sensing of cloud properties, which is the main topic of the present work. One point of interest derives from the fact that the imaginary part of the refractive index of ice presents a local minimum around 450 cm^{-1}, while the real part has values comparable to those found in the main atmospheric window (Di Giuseppe & Rizzi, 1999). Due to reduced ice absorption at FIR, the radiance signal, observed by a ground based or by a hypothetical satellite sensor, originates deeper within the cloud, and therefore, additional information may be extracted with respect to conventional pas-

sive InfraRed (IR) instruments. At this purpose, Naud et al. (2001) state that the FIR bands around 410 and 550 cm^{-1} can be positively exploited for particle size identification in the presence of thick clouds; these signals can characterize large particles better than the 11- to 12-μm window band. Also, Yang et al. (2003) show that FIR spectral signatures of ice are useful in the retrieval of ice cloud properties from a satellite view: For example, they find that simulated Brightness Temperature (BT) near 400 cm^{-1} is sensitive to ice crystal size for optically thick clouds. In addition, the BT Difference (BTD) between 250 and 559.5 cm^{-1} shows very little variations with the particle size for thin clouds, but it is sensitive to optical thickness.

A general issue that has implications in a large number of physical processes is how atmospheric radiance, in presence of cloudy fields over extended spectral regions, that is, from shortwave to the IR wavelengths, is accurately simulated. Several studies have addressed this problem (among them are Bozzo et al., 2008, and Ham et al., 2009), and discrepancies have been found between state of the art simulations and measurements in cloudy conditions due to both the inadequacy of the scattering properties database and the inaccuracy in the description of the atmospheric and cloud state. The scarcity of measurements of ice clouds radiance fields at FIR has prevented to extend the testing of our current scattering properties databases down to 100 cm^{-1}. This paper aims at starting to fill this gap.

Recently, simulation quality at FIR wave number has been tentatively assessed in two pioneering studies based on few hours of cloudy field observations: Cox et al. (2010) and Maestri et al. (2014). In the study by Cox et al. (2010), measurements of mid-IR and FIR upwelling radiance above cirrus clouds are performed by the Tropospheric Airborne Fourier Transform Spectrometer (FTS) airborne sensor. The spectral radiances are then computed based on measurements of cloud Particle Size Distributions (PSD). The authors conclude that cloudy radiance simulations are not able to consistently reproduce the observed spectral radiances across the entire IR region, with particularly important discrepancies between 330 and 600 cm^{-1}. A possible cause has been identified in the inadequacy of sampling the cloud structure and the atmospheric state.

Maestri et al. (2014) present results concerning the first set of FIR spectral downwelling radiance measurements in presence of a thin midlatitude cirrus and in very dry atmospheric conditions. The cirrus cloud case was observed during the Earth COoling by WAter vapouR emission, ECOWAR-COBRA, campaign (Bhawar et al., 2008; http://www2.unibas.it/gmasiello/cobra/index.htm) through an extended experimental setup comprising the FTS REFIR-Prototype for Applications and Development (REFIR-PAD; Bianchini et al., 2006), other spectrometers and LIDARs, and a Vaisala radiosonde system. It is found that the differences between simulated and measured radiances in FIR microwindows (m-w) are larger for lower wave number channels and Cloud Optical Depth (COD) less then 0.5. With increasing COD, the differences are smaller but still larger than the total uncertainties that are related to the experimental conditions, scene variability, and poor knowledge of the atmospheric state. The analysis of the ECOWAR-COBRA cloudy data proved to be a pilot test study for the Antarctic deployment of the REFIR-PAD sensor, which will be described in this paper. Both Cox et al. (2010) and Maestri et al. (2014) analyze few hours of cirrus observations and refer to the specific atmospheric condition encountered during the experiment.

Till now, very few studies have been performed on microphysics of cirrus clouds in Polar regions, and in situ measurements of Antarctic cirrus properties are extremely rare. Remote sensing measurements from ground stations are particularly difficult in the Arctic regions because of the extreme experimental conditions. Nevertheless, the low values of water vapor concentration along the vertical profile offer the opportunity to better investigate the cloud microphysical properties, such as particle size, particle phase, and crystal habit. The results obtained from the present study will be compared to previous results retrieved from remote sensing measurements (i.e., Lubin & Harper, 1996; Mahesh et al., 2001; Stone, 1993) or in situ instrumentations (i.e., Hogan, 1975; Lawson et al., 2006; Lachlan-Cope et al., 2001; Walden et al., 2003), and possible different assumptions and potential causes of discrepancies will be discussed. The cited studies show a common result that on the Antarctic Plateau, thin cirrus-like clouds are observed at heights between 3 and 7 km above the ground level. Low clouds are also observed but less frequently. Large optical depth (larger than 5) are encountered in less than 10% of the cases.

The deployment of REFIR-PAD at Concordia Station on the high Antarctic Plateau at Dome C within the Italian National Program for Research in Antarctica (PNRA) represents the first long-lasting field campaign collecting high spectral resolution atmospheric radiance spectra in the FIR with continuity for an extended

period spanning many years, starting from the end of 2011 with the XXVII Antarctic scientific expedition (Palchetti et al., 2012; Bianchini et al., 2013; Bianchini et al., 2016).

The present work extends the research studies performed on the ECOWAR-COBRA limited data set to the analysis of a full year of downwelling atmospheric emission spectra, measured by the REFIR-PAD between December 2012 and December 2013 within the Radiative Properties of Water Vapor and Clouds in Antarctica (PRANA) experiment (Palchetti et al., 2015). Selected cirrus cloud cases (based on the availability of ancillary information and quality of the radiance signal) are extracted from the whole radiance database collected during the PRANA experiment and then analyzed. The analysis process takes advantage of the results obtained from the study of clear-sky radiances from the same REFIR-PAD data set (see Rizzi et al., 2016).

Two main objectives are pursued:

- First to set up a cloud detection and classification algorithm capable to exploit high-resolution data in the FIR. The algorithm is set to identify, in particular, thin cirrus clouds which are difficult to observe from conventional satellite measurements at high latitudes. In this context, the information content of the FIR concerning ice clouds is highlighted.
- Secondly to retrieve microphysical properties of nonprecipitating Antarctic ice clouds and, for the first time, characterize their radiative signature in the FIR part of the spectrum by using state of the art radiative transfer tools and an up-to-date database of ice crystal scattering properties.

The paper is divided in four sections. The experimental campaign including the instrumentation and the measured data set with error analysis is described in section 2. Section 3 concerns the preprocessing of REFIR-PAD data and the data selection. A methodology for the discrimination of clear and cloudy spectra and the classification of precipitating and nonprecipitating clouds is provided in section 4. Finally, section 5 analyzes the retrieval of cloud properties and the radiance simulation methodology and discuss the results.

2. Antarctic Campaign Setup

Data analyzed in the present work are collected at the Italian-French research station of Concordia, located on the Antarctic Plateau at Dome C (75° 06′ S, 123° 23′ E) at 3.233 m a.s.l. Several scientific objectives are pursued by this experiment (Liuzzi et al., 2014; Rizzi et al., 2016; Di Natale et al., 2017). Among them, of our interest, is the study of clouds and the improvement of radiative transfer forward models and retrieval methodologies with particular attention devoted to the underexplored FIR region. A detailed description of the instrumentation used for the field campaign can be found in Palchetti et al. (2015), just a brief overview is given here.

Spectral measurements of the downwelling radiance are performed by REFIR-PAD, which provides spectrally resolved zenith-sounding radiance measurements in the 100–1,400 cm^{-1} range with a 0.4 cm^{-1} resolution, thus covering a large part of the atmospheric longwave emission including either the FIR and part of mid-IR region. REFIR-PAD is a fast scanning spectro-radiometer with signals acquired in the time domain and resampled in postprocessing at equal intervals in optical path difference. It has been designed to operate with uncooled detectors and optics; it operates 24 hr/day, alternating cycles of about 6 hr of measurements, during which 27 sequences of observations are typically collected, with 3 hr of analysis. The instrument is installed in a shelter devoted to atmospheric physics that is located 500 m southward from the main station, in the so called "Clean Air Area," where the predominant winds keep the air clean from the exhausting plume of the power generator.

When available, cloud characterization is obtained with a tropospheric LIDAR system (Ricaud et al., 2017) installed in the same shelter used for REFIR-PAD. The instrument, operating there since 2008 for several PNRA programs (TAVERN, ICE-CAMERA, PRE-REC, and PRANA), provides tropospheric profiles of backscattering and depolarization signal with a vertical resolution of 7.5 m from 30 to 12,000 m above ground level (agl), every 5 min, 24/24 hr, by means of a fully automated system. For the present work, quick-looks daily images are used, covering the entire 2013 that can be downloaded online (http://lidarmax.altervista.org/lidar/home.php). In addition to quick-looks, for selected days, digital backscattering data were provided to improve the detection accuracy of the base and top height of the cloud layers.

A Vaisala WXT520 weather station is installed on the roof of the same shelter, providing daily observations of local meteorological conditions. Routine radiosondes observations are performed at the station every day

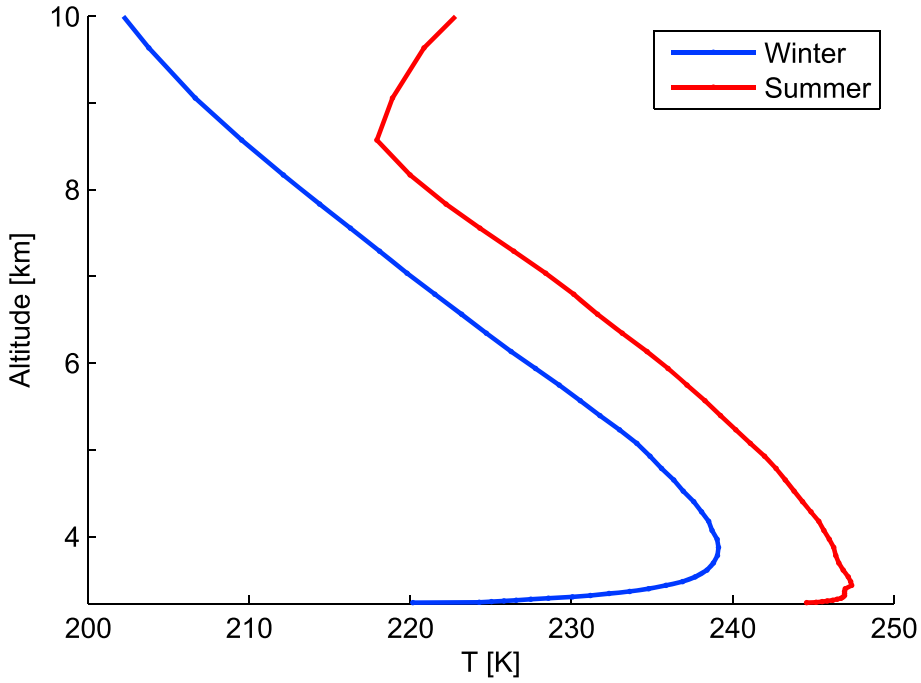

Figure 1. Averaged temperature profiles in presence of cirrus clouds. Austral Winter and Summer cases are derived from a total of 26 case studies.

at 12 UTC by Vaisala RS92 sondes. The radiosonde's data do not suffice to fully characterize the entire atmospheric profile time series. Since the knowledge of the atmospheric profiles of temperature, pressure, and gases concentrations are fundamental for the retrieval of cloud parameters, an extended data set is obtained using the European Centre for Medium-range Weather Forecasts (ECMWF) analysis for the Dome-C site, containing four atmospheric profiles every day at 00, 06, 12, and 18 UTC. Same time interpolation and layering procedures used for clear sky analysis (Rizzi et al., 2016) are adopted. As an example in Figure 1, the mean temperature profiles for the winter and summer days in presence of clouds are plotted. Note the temperature inversion near the ground in both cases. Typical values of water vapor column range between 0.1 and 1.1 mm, with an average value of 0.6 mm for summer cases and 0.4 mm for winter ones. The selection of cloud cases is described in the next paragraph.

3. Ice Cloud Classification

Antarctic clouds case studies can be selected in accordance with meteorological conditions under which they were observed only after an accurate cloud classification. For this reason, a supervised procedure was implemented in order to classify spectra as clear or cloudy and identify precipitating and not precipitating clouds. The mathematical algorithm of the classification method is described in details in Rizzi et al. (2016) and used to select the clear sky cases. Here only the general characteristics of the algorithm are outlined, and examples regarding the cloud classifications are provided. The full algorithm, called Cloud Classification for REFIR-PAD (CCREF), is characterized by a three-step procedure:

1. First, spectra collected over a time interval of about 3 months are grouped together. For each of them, measured radiance in narrow spectral bands (mostly m-w both in the IR and FIR spectral intervals) are converted into BTs. The complete list of central m-w wave numbers and their spectral widths are given in Rizzi et al. (2016). Each REFIR-PAD full radiance spectrum is replaced by BTDs obtained for each pair of m-w. The BTDs are called "features" since they are used to describe the spectral characteristics of the observed scene.
2. Second, a supervised features selection algorithm is applied with the objective to find out the most sensitive BTDs for the discrimination between different types of spectra (e.g., clear and cloudy scenes). A training data set is built on a monthly basis, and its elements undergo an a priori classification/identification by means of LIDAR observations. In fact, the training data set is built based on LIDAR quick-looks of

Table 1
"Features" Selected to Discriminate Ice Clouds From Liquid Water Clouds

Interval at (cm^{-1})	Interval at (cm^{-1})	Occurrences	Type
840.0	900.0	40	WIN-WIN
381.2	390.0	27	FIR-FIR
573.2	870.0	20	FIR-WIN
438.4	478.8	16	FIR-FIR
573.2	840.0	14	FIR-WIN
410.4	449.6	10	FIR-FIR

Note. Features are the Brightness Temperature differences at the wave number channels indicated in columns 1 and 2. The features selection algorithm is run 10 times considering four different combinations of Austral summer months (D-J-F, J-F, D-J, and D-F). The features total number of occurrence is reported in column 3. Column 4 indicates the type of channel used to the define the feature (WIN stands for the main infrared windows 800–1,000 cm^{-1}, while FIR (Far InfraRed) refers to the 100–600 cm^{-1} interval).

the backscatter coefficient that is sensitive to the presence of water (liquid and frozen) particles, while LIDAR depolarization ratios are exploited to distinguish the liquid phase clouds from ice clouds. During summer months, water cloud layers, characterized by a low depolarization ratio, are detected by the LIDAR at altitudes that can be higher than 1,000 m agl. These clouds are mainly composed of supercooled water droplets and can be observed even at almost −40 °C (below this temperature, homogeneous nucleation occurs, and only ice clouds exist; Liou & Yang, 2016). These water clouds often resolve in ice crystal precipitation, as observed from LIDAR data.

Data taken at different times (months) are combined together for multiple runs of the features selection algorithm. The algorithm is run 10 times for each combinations of data in order to extract the most statistically significant features capable to classify the observed scenes in terms of cloud presence, phase, and type. Results are shown in Table 1 for the cloud phase classification. The most recurrent BTDs contain information related to the radiance spectral characteristic in the main IR window region, that is particularly important for the discrimination between ice and water clouds due to a different spectral behavior of the imaginary part of the index of refraction of water in the two phases (well documented in the scientific literature). Multiple combinations of a FIR and an IR window channels and of two FIR channels are also selected due to the strong difference between the absorption coefficient for water and bulk ice in the two spectral regions.

3. In the third and final step, the spectra, described by means of the selected features only, are ingested into a Support Vector Machine (SVM) algorithm that provides the final classification in three steps: separation of clear from cloudy spectra, ice from water clouds, and nonprecipitating from precipitating clouds. When the SVM process is run, the margin of the SVM is built using a nonlinear kernel in order to map the nonlinear problem to a higher dimensional space where it becomes linear. Mathematically, it is solved by implementing kernel function in the SVM (Theodoridis et al., 2010) that in our case are based on Radial Basis Functions (RBF). The RBF kernel adopted in this study are Gaussian, widely used for several applications (e.g., Melgani & Bruzzone, 2004) working with classification of remote sensing measurements. A free parameter (σ) that corresponds to the radius of the RBF is introduced. The parameter σ is a measure of the tuning: Small values of σ produce a strict local classification tuned on the training data set (and if too strict, the classification cannot be generalized), while very large values lead to flat classifiers. For this reason, the choice of the σ value is critical; it must both minimize empirically the test errors and allow a sensible classification (Theodoridis et al., 2010). An example of SVM result is shown in Figure 2, obtained considering data from December 2012 and January and December 2013 that turned out to be the month with the largest occurrence of water clouds. For this trimester, the σ value is set to 5. Similar values are used for the other trimesters considered. The algorithm demonstrates an excellent ability to discriminate between cloud phases. Note that the figure shows the scatter plot of only the first two features selected by the algorithm; the final classification is performed considering all the selected BTDs reported in Table 1. The number of spectra used for algorithm training and validation is of the order of 30–40 for each class (i.e., ice or liquid water clouds) in accordance with the trimester considered. This number corresponds to about 5–10% of the total of the identified cloudy spectra for each trimester.

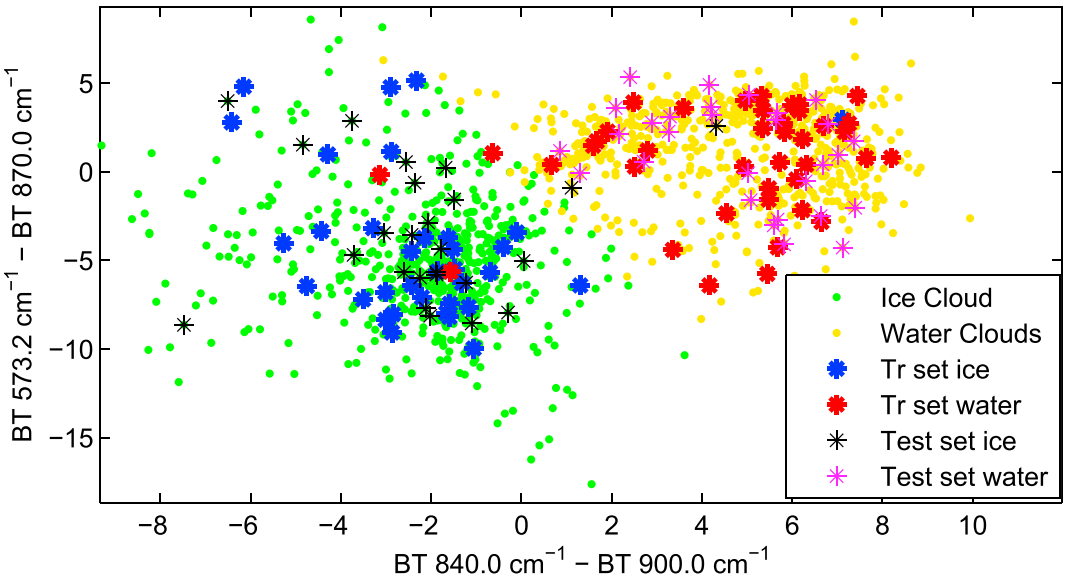

Figure 2. Example of Support Vector Machine for water phase cloud classification: scatter plot for a data set comprising three summer months (December 2012 and January and December 2013), with training (Tr set in the legend) and test (Test set in the legend) examples superimposed. BT = Brightness Temperature.

The accuracy of the classification algorithm is evaluated by comparing the classification results to LIDAR quick-looks. Performances are excellent, but failures occur in presence of clouds with small COD: For these cases, spectra of either liquid or ice water clouds are very similar to clear ones, and further investigations are needed to improve the classification. Typical training and test validation errors for the clear/cloudy identification are of 2–5%. For the cloud phase classification, the errors raise to about 5–10% of the total cases analyzed, while for the classification of ice cloud type (precipitating or not), it is, generally, of the order of 10–20%; the highest values are found in October and November 2013. Specifically, in the example of Figure 2, the training set error is 3%, and the test validation error is 4%.

In Figure 3, the results of the classification algorithm applied to the whole data set comprising a whole year are reported; about 13,500 REFIR-PAD spectra were analyzed. First, SVM identifies spectra as cloudy or clear (left panel), with measurements that fall inside the margin between the two groups labeled as unclassified

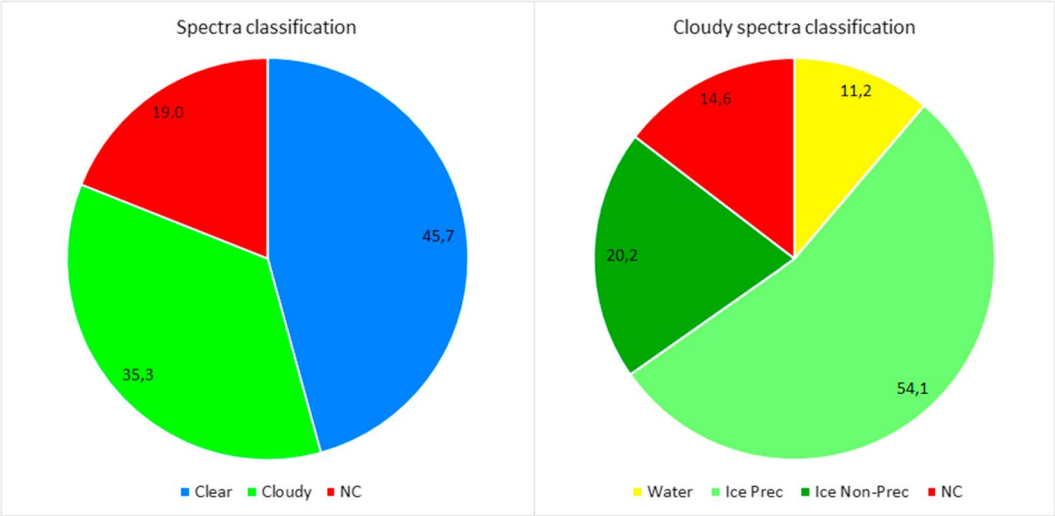

Figure 3. Results of the classification algorithm applied to the whole 2013 data set. (left) Spectra are identified by the Support Vector Machine algorithm as Clear or Cloudy or Unclassified (NC). (right) Classification of cloudy spectra in liquid phase clouds, ice clouds nonprecipitating, ice clouds associated to precipitation, and NC cases.

Table 2
Main "Features" Selected to Discriminate Precipitating From Nonprecipitating Ice Clouds

Interval at (cm^{-1})	Interval at (cm^{-1})	Occurrences	Type
559.2	573.2	52	FIR-FIR
238.4	381.2	52	FIR-FIR
238.4	390.0	38	FIR-FIR
531.2	573.2	38	FIR-FIR
522.4	573.2	35	FIR-FIR
680.0	900.0	35	CO_2-WIN
573.2	900.0	30	FIR-WIN
573.2	870.0	29	FIR-WIN
238.4	410.4	22	FIR-FIR
680.0	870.0	19	CO_2-WIN

Note. The features selection algorithm is run 10 times for 23 different groups of months. FIR = Far InfraRed.

(NC). A very weak seasonality is detected (not shown). In fact, clear sky is predominant (52%) in the austral summer and slightly decreases in winter (47%). Clouds are detected in the 34% of the cases in summer and 36% in winter months. Note that the large number of unclassified cases (19%) is likely affecting the clear-cloud occurrence statistics.

On the right panel, cloudy spectra are classified into subclasses. This is the result of the final stage of the classification process focusing on ice clouds and aiming at separating data taken during precipitation from nonprecipitating conditions. Results show that the ice nonprecipitating clouds are observed in less than 7% of the all spectra. In this case the classification is particularly challenging, since spectral measurements do not always clearly separate between the two classes of observations. As a consequence, in the majority of the cases, the classification error reaches values at around 10% for the training data set and is even larger for the test data set. Selected features in this step involve generally 6 to 12 intervals; the random component of the process and the similarity in the spectral features of the precipitating and not precipitating ice clouds make the selected group of features vary at each iteration. Results obtained from 10 iterations for 23 pairs of months are shown in Table 2. In the majority of the cases, the chosen features correspond to BTDs between two FIR partial m-w regions. The 573.2 cm^{-1} is a so called dirty window (rotational absorption lines of water vapor molecules are present) that is frequently selected; this spectral region is one of the regions of maximum sensitivity to cloud signal, and in fact, it is chosen in at least half of the total number of runs. Also, another frequently chosen interval is the one at around 238.4 cm^{-1}, dirty window, with a large sensitivity to water vapor absorption. A possible explanation of why this feature is so important lies in the fact that precipitating and nonprecipitating conditions are differently affected by the water vapor mass profile. The overall training error of the SVM is much larger than for previous classifications, and detailed analysis of results indicates difficulties to discern faint precipitating clouds from nonprecipitating clouds with high COD due to the similarities of their spectral properties within the spanned spectral interval. Note also that many classification failures, up to 25%, are encountered at this last stage for spectra collected in October and November 2013, which are affected by higher values of instrumental noise, just before the instrument maintenance that occurred in the following December.

3.1. Ice Clouds Case Studies

From a combined analysis of the classification algorithm and the LIDAR quick-looks, 26 nonprecipitating ice cloud episodes are selected over the entire year 2013. LIDAR profiles are analyzed in order to evaluate the structure, temporal variability, and geometry of the cloud. For each case, one REFIR-PAD spectrum (i.e., the average of four consecutive acquisitions lasting 5.6 min) is used unless the scene is particularly stable. In this latter case, two or three spectra are averaged (using the same procedure adopted for clear sky; Rizzi et al., 2016) depending on the stability of observed scene.

Some examples of selected REFIR-PAD measurements are reported in Figure 4 on the LIDAR quick-looks with a superimposed black vertical bar indicating the occurrence time. The cases are examples of the diver-

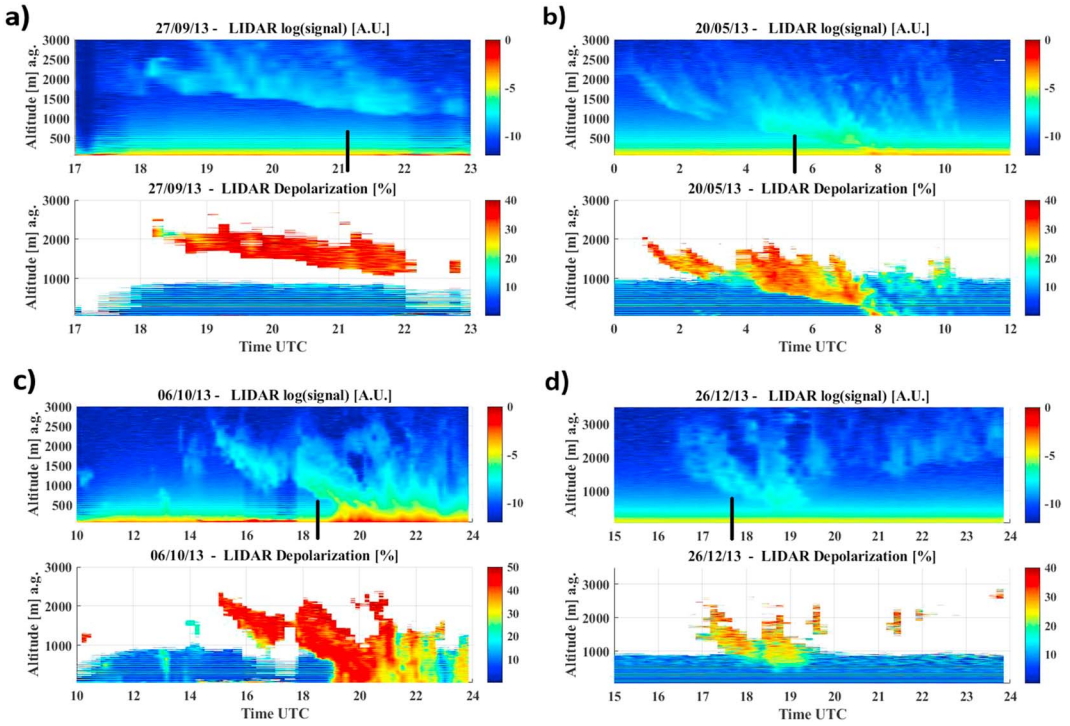

Figure 4. Examples of typical cloud events composing the data set. The backscatter coefficient and the depolarization ratio are reported. (a) High altitude, nonprecipitating thin ice cloud; (b and c) high altitude clouds followed by precipitation events; (d) falling ice crystals in midtroposphere not reaching the ground. The black vertical lines indicate the time of the selected REFIR-Prototype for Applications and Development spectrum. Dates (upper left corner of each plot) are expressed in day-month-year. Black vertical line indicate selected REFIR-Prototype for Applications and Development measurements times. Note that the multiple horizontal straight lines are caused by ringing noise as induced by the laser firing in the first part of the LIDAR signal. At the time of the LIDAR measurements, the S/N ratio was quite low due to a reduced laser power.

sity of conditions analyzed during the campaign. The case in Figure 4a is representative of a thin high cloud that does not lead to any precipitation events in the following hours. Such types of clouds are generally difficult to observe from satellite sensors because of their thin vertical extent and small optical depth and because of the similarity in their radiative properties with those of the background (that from the satellite view is the frozen or snow-covered ground). Figures 4b and 4c show two selected clouds characterized by nonprecipitating conditions (the analyzed radiance spectrum is chosen from this time lapse) followed by a time of solid precipitation. From the backscatter values measured by the LIDAR and reported in the plot, it is possible to note that cloud base height gradually decreases until falling ice crystals reach the ground. These situations are quite frequent in the Antarctic plateau and occur during all seasons. Finally, Figure 4d shows a cloud characterized by precipitating ice-crystals in midtroposphere but not reaching the ground.

Selected cases generally fall within one of these typologies, with bottom height lying between 500 and 3,500 m agl as for the case of the highest detected cloud case on 02 January 2013. The typical cloud geomet-

Table 3
Mean Geometrical and Physical Properties of the 26 Selected Nonprecipitating Ice Cloud Case Studies

	All	Summer	Winter
Mean cloud base height (m agl)	1,450	1,650	1,350
Mean cloud base temperature (K)	236	239	230
Mean vertical extent (m)	1,050	1,000	1,100
N cases	26	6	5

Note. Characteristics of summer and winter cases only are also reported.

rical depth is of the order of 1,000 m, except for a pair of very thin cloud cases. For the cloud case occurring on 26 December 2013, the vertical thickness measured by the LIDAR is of 400 m; for one case, the vertical extent is around 1,500 m which is the thickest case in the selected data set. Some basic information about cloud averaged properties are resumed in Table 3.

4. Microphysical Assumptions and Radiative Computations Setup

Lacking of in situ data about crystal shapes composing the selected clouds, a priori assumptions on particles' habits need to be adopted. It has been demonstrated (Maestri & Holtz, 2009) that the radiance sensitivity to crystal shape is very low in the main atmospheric IR window (from about 800 to 1,000 cm^{-1}) and the radiance spectral variation mostly depends on crystal size (i.e., cross section) and total optical depth. Thus, a retrieval of the shape of the ice particles contained in cirrus cloud layers is particularly challenging only using radiance at these wave numbers (and in general from conventional IR passive measures). Particle habits are usually assumed as a priori information in cloud property retrievals exploiting remote sensing measurements. Nevertheless, radiance sensitivity to crystal shape is expected to be larger in the FIR where the imaginary part of the index of refraction of ice decreases, in particular at around 450 cm^{-1}, and scattering processes become more important. At what stage this habit effect is important is evaluated for the considered experimental conditions in the following. For this reason, the retrieval of cloud properties (particles size and optical depth) exploiting the main IR window is performed multiple times in accordance with the a priori assumption on the particles' habit (see next paragraph). Since this process is very time-consuming, the number of crystal shapes used as a priori assumption might be limited, and the choice of the habits has to be the more realistic as possible and based on the available experimental data or, as in the present case, on climatology.

Bailey and Hallett (2009) present an up-to-date review of atmospheric ice crystal shapes, based on extensive field measurements and laboratory simulations. A comprehensive habit diagram that describes the shapes of atmospheric ice crystals as a function of temperature and ice supersaturation is reported. The authors point out that ice crystal habit is mainly a function of temperature, while supersaturation plays a secondary, but not negligible, role. Analyzing thousands of cloud particle imager observations, the authors find that clouds whose tops are warmer than approximately −40 °C are mainly composed of plate-like polycrystals, while clouds with tops at temperature below −40 °C usually have a habit distribution dominated by columnar polycrystals, including bullet and mixed rosettes. Moreover, laboratory observations indicate that bullets rosettes and columnar shapes are not likely to nucleate at temperature approximately above −40 °C, even if short columns rarely appear throughout the plate-like region. As a consequence, the authors suggest that bullet rosettes shapes should not be used in general to model clouds at temperature above −40 °C. This threshold is shown to be a real habit transition point from predominantly plate-like (−20 to −40 °C) to columnar habits, down to −70 °C. However, at very low ice supersaturation levels, crystals generally show a reduced temperature dependency, with compact faceted polyhedral shapes or short columnar ones. Laboratory crystals, grown in static conditions, show shapes that match the in situ observations if sedimentation or updraft is negligible. On the contrary, substantial changes in atmospheric crystal shapes are observed when vertical motions occur. For example, when bullet rosettes or columns precipitate in a warmer cloud region, their aspect ratio tends to reduce, becoming mixed rosettes with plate-like components.

More specifically on Polar clouds, a wide range of crystal shapes and dimensions is observed from the scarce measurements at continental and coastal sites in Antartica (Lachlan-Cope, 2010). Among them, it is worth mentioning the work from Walden et al. (2003) that collected, at the ground, a large data set comprising the dimensions of about 20,000 crystals during the Antarctic winter of 1992. They observed nine different types of ice crystals with a predominance of columns (hexagonal prisms) or hexagonal plates for diamond dust events. Note, in fact, that on the Antarctic plateau, ice crystals are often observed in the atmosphere close to the surface as clear sky precipitation. These particles are generally larger than cloud particles. They also observed blowing snow particles (almost rounds) and snow grains precipitating from clouds. Lawson et al. (2006) report about two Antarctic campaigns of ice crystal collection at the ground, which were classified on habit base: 30% of the particles were found to be rosette shaped, 45% were diamond dust (typically made by columns, thick plates and plates), and 25% had an irregular shape.

Based on these findings, considered the difficulty in making any a priori assumption and aware of the extreme dry conditions on the Antarctic Plateau, all the simulations presented are made assuming two pris-

tine ice crystal habits and two composite shapes. The pristine shapes, chosen from the Yang et al. (2013) database, are hexagonal columns and plates. The complex habits (also from Yang et al., 2013) are bullet rosettes and aggregates of eight columns (called aggregates for simplicity). This last shape is chosen to be consistent with the C6 MODIS Cloud Properties Product where ice clouds are assumed to be composed of a gamma distribution of aggregated columns (http://modis-atmos.gsfc.nasa.gov/Webinar2014/MODIS_Atmo_Webinar9_Platnick.pdf).

For each of the four considered habit types, both the retrieval and forward simulations are performed. As mentioned, the radiative properties are derived from Yang et al. (2013) that developed a spectrally consistent data library containing the scattering, absorption and polarization properties of a set of 11 randomly oriented ice crystal habits at wavelengths from 0.2 to 100 μm. The maximum dimension of each habit ranges from 2 to 10,000 μm, spanned by 189 discrete values. Information relating to the volume and projected area of each habit as well as the asymmetry parameter, single-scattering albedo, extinction, and absorption cross sections and the six independent elements of the phase matrix are provided. The effect of surface roughness is also considered with the introduction of a parameter that assumes values of $\sigma = 0$ for smooth particles, $\sigma = 0.03$ for moderately rough particles, and $\sigma = 0.5$ for severe surface roughness. A set of preliminary simulations is performed to understand the radiance sensitivity to the roughness parameter in the FIR spectral region and atmospheric conditions similar to what found during the PRANA campaign. In particular, the roughness effects are evaluated at wave number where the scattering process are quite relevant (i.e., at around 400 cm^{-1}). Hexagonal column (as defined in the Yang et al., 2013, database) and the minimum and maximum surface roughness are used. The differences in downwelling-simulated REFIR-PAD radiances (not shown here) are less than 0.1% of the radiance value and, for this reason, negligible with respect to the spectral instrumental uncertainties, that, in the same wave number range, are larger than 1 $mW{\cdot}m^{-2}{\cdot}sr^{-1}(cm^{-1})^{-1}$ (hereinafter indicated as "radiance unit"). As a consequence, for all the computations (direct and inverse), the roughness parameter σ is set equal to zero.

Bulk cloud properties are computed assuming a set of gamma-type PSDs (26 are considered in the database). The modified gamma PSD is defined as

$$n(D) = N_0 D^{\mu} e^{-\lambda D}, \tag{1}$$

where D is the particle's maximum dimension, and μ identifies the spread of the distribution and is kept fixed in our database to a value equal to 7 that, being positive, makes the PSD to assume an under exponential shape. λ is called the slope of the PSD, and for each ice crystal shape, 26 slopes are considered that identify 26 different effective particles dimensions. N_0 is the intercept of the gamma distribution and linked to the total number of particles in the PSD. This parameter does not change the shape of the PSD (in a $D - N(D)$ graph) and thus does not affect the spectral features of the bulk radiative properties but only shift their values up or down consistently. The spectral behavior of the PSD bulk optical properties is uniquely identified by three parameters: crystal habit, λ, and μ (this last is assumed fixed).

A general formulation for the effective dimension, D_{eff}, of a PSD of nonspherical particles was introduced by Foot (1988):

$$D_{\text{eff}} = \frac{3}{2}\frac{IWC}{\rho_i \int_{D_{\min}}^{D_{\max}} P(D)n(D)\mathrm{d}D} = \frac{3}{2}\frac{\int_{D_{\min}}^{D_{\max}} V(D)n(D)\mathrm{d}D}{\int_{D_{\min}}^{D_{\max}} P(D)n(D)\mathrm{d}D}, \tag{2}$$

where $P(D)$ and $V(D)$ are the projected area and volume of a particle with maximum dimension D, respectively, while ρ_i is the bulk ice density, assumed constant.

When comparing results concerning the dimension of PSDs composed of different habits, it should be noted that even if the effective dimension is the same, the PSDs are different due to the fact that the $V(D)/P(D)$ ratio depends on the habit type. In other words, different habits might have the same D_{eff} with different PSDs.

Radiative transfer computation are performed with the RTX code (Rizzi et al., 2007) that is an extension of the RT3 doubling and adding code introduced by Evans and Stephens (1991). RTX is a plane parallel, line-by-line multiple scattering radiative transfer algorithm used as a reference tool for faster radiative codes (Bozzo et al., 2008), for validation/calibration experiments (Maestri et al., 2010), for theoretical studies

(Harries et al., 2008), for cloud properties studies (Bozzo et al., 2010), and in support of cloud properties retrievals (i.e., in Maestri et al., 2014).

High spectral resolution radiative transfer computations in presence of multiple scattering layers are time-consuming. An a priori analysis concerning the expansion of particles phase function in terms of Legendre polynomials is required as a compromise between model accuracy and computing time. Maestri et al. (2014) show that using $nz = 16$ zenith angles for each hemisphere is insufficient to obtain an accurate computation of the radiance spectral field, especially in presence of ice particle with large dimensions. The number of zenith angles used in the radiance field computations affect the representation accuracy of the phase function that is expanded in terms of Legendre coefficients (nc). Using a Gauss-Legendre quadrature scheme implies that $nc = 4 \cdot nz - 3$. For the present work, all the forward and inverse computations are done using $nz = 60$, and thus, the Legendre coefficients are $nc = 237$ that allows a model error far below the measurement uncertainties.

The retrieval of selected cloud properties is performed using an updated version of the RT-RET method whose basics are described in Maestri and Holtz (2009). The layer-to-sensor spectral gaseous transmittances are required as RT-RET input, together with surface temperature, and cloud top and bottom heights that are derived from time coincident LIDAR observations using a simplified methodology similar to the one reported in Pal et al. (1992). The algorithm assumes that the vertical distribution of ice mass content is described by a climatological profile, typical of cirrus clouds (Veglio & Maestri, 2011). In situ measurements are usually used to define the first guess information concerning the cloud microphysics (size distribution parameters and crystal habit), but since this information is not available for PRANA, four different habits are assumed separately, as previously discussed.

In RT-RET, a first guess information concerning the cloud scattering properties is used in the algorithm to perform a first iteration of the cloudy simulation. Simulated radiances are fitted to the measured radiances in selected microwindow channels in the 800–1,000 cm^{-1} region (using a nonlinear convergence methodology). From fitted radiances, retrieved spectral absorption Optical Depth (OD) is derived that has been showed to be minimally dependent on the assumed first guess scattering properties in that spectral band. The retrieved cloud spectral absorption OD is then compared (via a root-mean-square fitting method) with a precomputed database of absorption OD representative of multiple PSDs (identified by their effective dimensions). A single set of bulk scattering properties is thus selected. The optical properties retrieved in the first iteration are used as the second-guess scattering properties to initialize RT-RET for the second iteration that is similar to the first one with the only difference being the updated scattering properties. This second iteration allows a convergence to a spectral OD independent of the first guess, and finally, the cloud total OD and microphysical properties (PSD effective dimension) are retrieved (Maestri & Holtz, 2009).

Results from an IR cloud property retrieval procedure, such as RT-RET, are affected by uncertainties originating from multiple sources such as forward model accuracy, the ice-crystal database's uncertainties, measurement noise, lack of knowledge about atmospheric and surface properties, and assumptions made in the algorithm. As shown by Maestri and Holtz (2009), the errors associated with the algorithms and the database are very small with respect to those produced by assumptions in the retrieval code and by the a priori knowledge of the atmospheric state: Inaccuracies in the definition of the cloud geometrical properties (associated with cloud temperature) dominate the uncertainties in the retrieved COD. In all our computation the cloud geometrical structure is retrieved from colocated LIDAR measures, and thus, this source of error is minimized. The surface properties (skin temperature and spectral emissivity) have a negligible impact for an up-looking geometry as shown in Maestri and Holtz (2009). Anyway, skin temperature is derived from the meteorological station on-site and the surface emissivity is that one of the ice (Huang et al., 2016). Detailed information concerning the water vapor profile are very important in the up-looking configuration since water vapor absorption/emission properties primarily affects the radiance pattern originating in layers between the surface and the cloud. As reported in section 2, temperature and humidity profiles are derived from radiosonde measurements and from the operational analysis of ECMWF Meteorological Archival and Retrieval System archive. These profiles are given at the model levels (91 from 1 January 2013 to 25 June 2013 at 18 UT and 137 from 26 June 2013 onward), and all model level pressure values can be computed from the surface pressure. Radiosonde data are used for selected spectra measured within 70 min from the daily radiosonde launch (12 UTC). Otherwise, an interpolation between radiosonde data and ECMWF

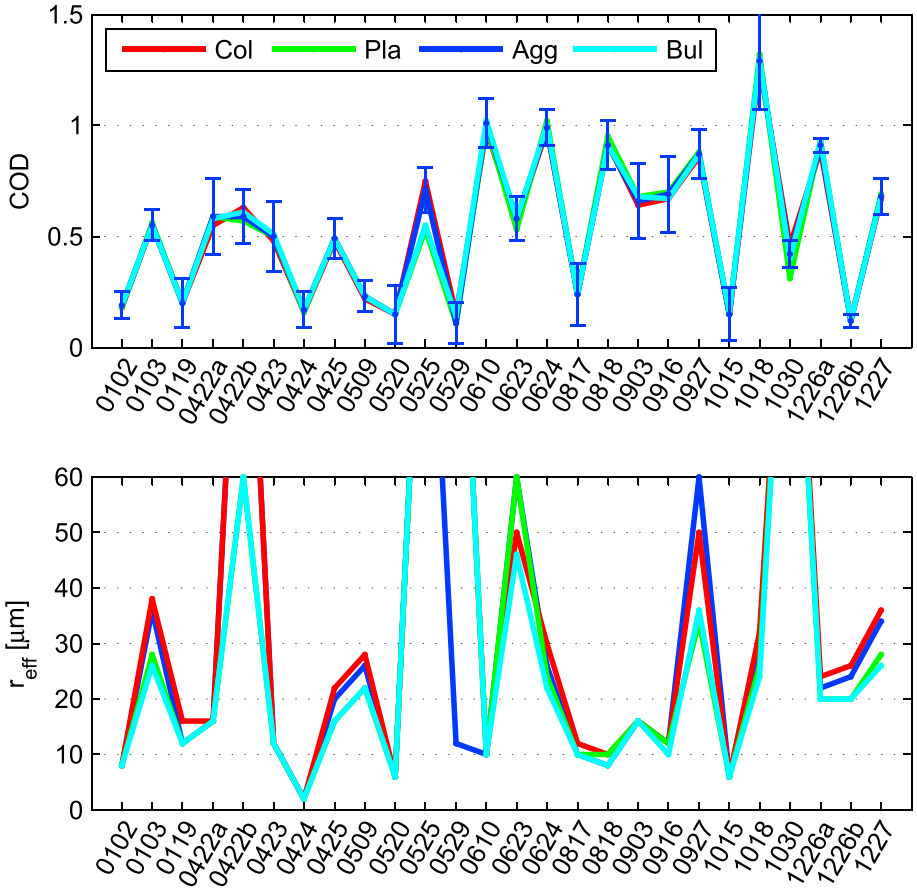

Figure 5. Retrieved CODs (upper panel) and effective radii, $r_{eff}=D_{eff}/2$, (lower panel) versus time (as month and day, MMDD, of year 2013) for all the 26 cirrus cloud cases. Results are obtained for four habit assumptions as reported in the legend. The letters a and b in the dates indicate different cloud cases occurring on the same day. In the upper panel, the retrieval uncertainties related to COD are also plotted (see Maestri et al., 2014). In the lower panel, the r_{eff} values obtained for the cases 22 April (b), 25 May, and 30 October 2013 is 120 μm in almost all of the habit assumptions and is kept out of y axis range for visual purposes. COD = Cloud Optical Depth.

data is performed. ECMWF analysis are used in any case to fill the radiosonde measurements gaps at high atmospheric levels.

Note that RT-RET is based on the same forward model used for the forward simulation (RTX) so that the inverse and direct computations are completely coherent.

5. Results and Discussion

5.1. Cloud Retrieved Properties

Microphysical and optical properties have been retrieved, using the RT-RET methodology, for the 26 case studies of nonprecipitating cloud selected as discussed in section 3. Retrieved CODs versus time are shown in Figure 5 (upper panel) for the selected habits. CODs (at 900 cm^{-1}) show the same retrieved values independently of the assumed ice crystal shape except in three cases when the retrieved effective radii are the largest value, 120 μm included in the database (see the end of this paragraph). COD values range between 0.1 and 1.3 and are in the range of those found by Stone (1993) and Mahesh et al. (2001) in their studies about Antarctic clouds.

Stone (1993) presents results from eight cases of winter clouds at the South Pole Station, using data collected during several flights of a radiometersonde that measures upward and downward IR irradiances. Detected clouds are generally optically thin with integrated COD in the IR of the order of unity or less and bottom heights placed at the level of temperature inversion close to ground. Mahesh et al. (2001) analyze cloud cases from a campaign conducted at South Pole Station in 1992, during which the longwave atmospheric emission

Table 4
Literature Results in Terms of Retrieved or Computed r_{eff} or, Where Specified, Equivalent Radii for Collected Ice Crystal PSDs (Adopting Equal V/A Spheres Formulation), Together With RT-RET Obtained Values

Authors	R (μm)	Notes
Lubin and Harper (1996; AVHRR)		(50 μm was the maximum retrievable dimension)
	12.3	Mean value for summer months
	5.6	Mean value for winter months
Stone (1993; radiometersonde)	4–16	Mean value over eight summer clouds (all crystals)
Mahesh et al. (2001; ground-based FTS)	15.2	Median remote sensed value over the entire year (25 μm is the maximum retrievable dimension)
Walden et al. (2003; ground-collection)	10.1	Mean value for column crystal PSD and winter months
	15.1	Mean value for plate crystals PSD and winter months
	25.2	Mean value for bullet clusters PSD and winter months
Lawson et al. (2006; ground-collection)	10.5	Mean equivalent sphere radius column crystals PSD, summer months
	19.2	Mean equivalent sphere radius, plate crystals PSD, summer months
	28	Mean equivalent sphere radius bullet rosettes crystals PSD, summer months
Shimizu (1963)	100	Long column crystal at surface (diamond dust)
Lachlan-Cope et al., (2001; ground disdrometer/Formvar replicas)	20–200	All crystals at the surface
PRANA year 2013 (ground-based FTS)	25	Mean value for columns, all cases
	20	Mean value for plates, all cases
	19	Mean value for bullets, all cases
	25	Mean value for aggregates, all cases
	16	Median value for all the habits

Note. AVHRR = Advanced Very High Resolution Radiometer; PSD = Particle Size Distributions; FTS = Fourier Transform Spectrometer.

spectra are measured twice a day. Measurements are taken from the surface by means of a FTS at 1 cm^{-1} resolution. A year-long data set of cloud properties representative of the Antarctic Plateau is presented, and seasonal variations of the derived parameters are highlighted. Clouds with optical depth between 0 and 1 are found in the 65% of the observed cases, while only the 24% of the total has a COD ranging between 1 and 5. Separating observations for the winter and nonwinter months, they found that CODs greater than 5 are twice as common in nonwinter months than in winter months.

Results from the PRANA database do not show any clear seasonal signal in terms of COD (independently of the assumed shape). One reason might be the small changes in the midlevel temperature of the observed clouds during the varying season. In fact, the averaged mean cirrus temperature is 238.5, 230.8, 231.9, and 234.7, respectively, for the trimester December, January, and February; March, April, and May; June, July, and August; and September, October, and November. When the clouds OD is analyzed as function of the cloud mean temperature, we derive a mean COD of 0.38 for temperatures lower than 230 K, while for higher temperatures, the mean COD is 0.59. The values are provided for the aggregates assumption but remains qualitatively valid for all the shapes, thus suggesting a correlation between mean cloud temperature and optical depth.

Retrieved r_{eff} (defined as $1/2 \cdot D_{\text{eff}}$) versus time are shown in the lower panel of Figure 5 where, again, the same a priori assumptions on crystal habit are adopted. Results exhibit a large variability: Values range from 2 μm up to 120 μm, spanning the whole range covered by the synthetic PSD data set. No significant seasonal trend concerning particle's dimensions is observed. Selected cases refer to very different cloud types, and this heterogeneity among case studies prevents the possibility to observe a clear seasonal signal, as instead discussed by Mahesh et al. (2001). As in the case of the COD, a difference is observed when cold cirrus (mean temperature lower than 230 K) are analyzed separately from warmer ones. For cold clouds, the mean

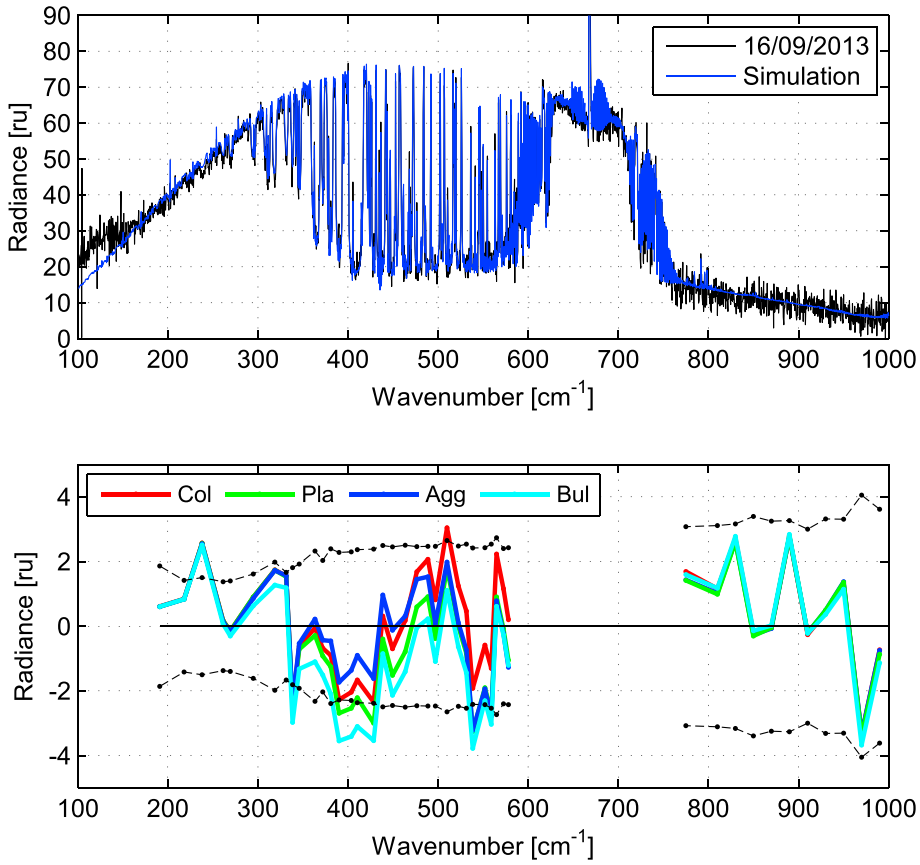

Figure 6. (upper panel) Measured spectra for the 16 September 2013 (black line) and simulated (blue line) data using aggregate crystals. (lower panel) Residuals (simulation minus measures) averaged over selected microwindows for all the four crystal shapes. The measurement error in each microwindow is shown as black dashed line.

effective radius detected (for the aggregates assumption) is 19 μm, while for the warmer clouds is about 35 μm.

Some studies report a time average of retrieved effective radius. One of the most significant work is the measurement campaign described in Mahesh et al. (2001). The retrieval methodology combines cloud's emissivity at 903 and 988 cm^{-1} and cloud's transmissivity in the 9.6-μm ozone band to determine the particle effective radius. Simulations, performed using Mie theory and the Discrete Ordinate Radiative Transfer code for a number of different effective radii and COD values, are compared with observations to obtain the best fitting r_{eff} and COD. The obtained median value of the retrieved r_{eff} is 15.2 μm.

Lubin and Harper (1996) estimate effective cloud particle dimensions using the Advanced Very High Resolution Radiometer channels at 11 and 12 μm; this study was conducted in conjunction with ground-based measurements reported in Mahesh et al. (2001) in order to derive independent information about clouds from two different viewing geometries. Mie theory is used to calculate optical properties for ice crystals, and about 300 satellite data sets are exploited to retrieve ice cloud properties. Results show a mean r_{eff} of 12.3 μm in summer and 5.6 μm in winter. These values are smaller than those found by Mahesh et al. (2001) over the same period. They suggest that this discrepancy may be due to smaller crystals at cloud top than at cloud bottom. A clear seasonal cycle is found, since derived ice summer crystals are larger than winter ones.

Stone (1993) uses Mie theory to simulate the measured IR irradiances. The comparison of measured and simulated spectra shows that the effective particle radius (r_{eff}) ranges between 4 and 16 μm and IWCs between 0.3 and 6 mg/m^3.

As mentioned, Walden et al. (2003) measured and cataloged the mean radius of diamond dust. They report mean effective radii for different shapes: solid columns (10.1 μm), plates (15.1 μm), pyramids (9.4 μm), and hollow columns (6.4 μm).

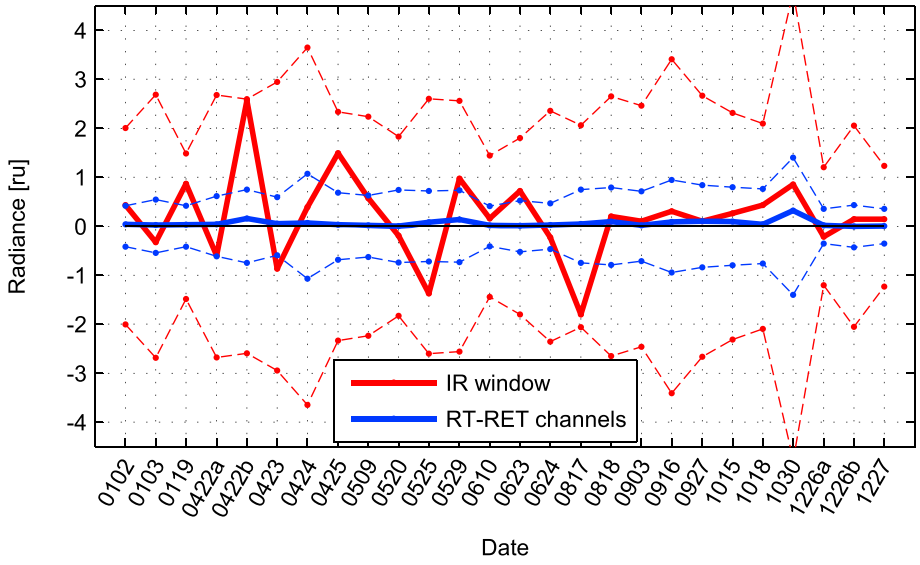

Figure 7. Differences between simulated (using aggregates) and measured radiances averaged over the 800–1,000 cm^{-1} interval. The differences calculated only for the channels used in the RT-RET retrieval are also shown. Dashed lines refer to the mean measurement error over the IR windows and over the RT-RET channels. IR = InfraRed.

Table 4 reports some of the results obtained by these authors together with our retrieved results (PRANA 2013). Mean effective values reported in the literature span from 5 to 27 μm depending on crystal habit assumption and season of observation. A direct comparison of the results from different campaigns is difficult. In fact, for example, Lawson et al. (2006) refer to mean values of equivalent sphere radii (i.e., the sphere with the same volume-to-area ratio of the correspondent ice crystal), while Walden et al. (2003) refer to effective radii for PSDs composed of equivalent spheres (Grenfell & Warren, 2010; Hansen & Travis, 1974). RT-RET values, averaged over all the available case studies, appear slightly larger than results from previous experiments. The mean value is sensibly affected by the large values retrieved (120 μm; i.e., the maximum value considered in the database) in three cloud cases (see legend of Figure 5). The latter cases are characterized by ice crystals falling down to about 500 m agl but not reaching the ground (sublimating during the fall). The median effective radius value of 15.2 μm computed by Mahesh through remote sensing data over the entire year is quite close to the median value obtained from RT-RET retrievals when assuming aggregates and column (for both about 20 μm) or for plates and bullets rosettes (about 16 μm).

5.2. Forward Simulations

Cloud retrievals discussed in the previous section are obtained from a limited number of window channels in the 800–1,000 cm^{-1} region. Forward simulations over the whole REFIR-PAD spectral range can be computed, using the retrieved cloud parameters, and the residuals between the simulated spectra and the measured ones are evaluated in the main IR and FIR windows.

In the upper panel of Figure 6, the measurement spectrum, collected on 16 September 2013, and the relevant simulation (using aggregate crystals) are shown as an example. The plot shows an overall agreement that is however difficult to quantify for each single REFIR-PAD channel, given the high variability of the measured signal, and therefore, the residuals are averaged over each m-w considered in the present study and are shown, for all selected habits, in the lower panel of the same figure. For some spectral intervals in the FIR, the residuals are larger than the measurement error.

The main IR window spectral interval must be analyzed separately from the rest of the spectrum because some channels are used in the retrieval process; hence, the residuals are expected to be smaller than in the rest of the spectrum. Figure 7 shows the mean residuals for channels used by the retrieval scheme (blue line) and the residuals averaged over all channels in the 800–1,000 cm^{-1} (red line). Residuals are very small for the RT-RET channels, with a slight general overestimation (of the simulation with respect to the measure) that depends on the initialization of the retrieval process. The mean residuals over the whole window interval is 0.85 radiance unit (in absolute value) corresponding to about 5% of the signal. Note that the radiance signal in this interval is very low, especially in the presence of the thinnest clouds, for which it is comparable to the

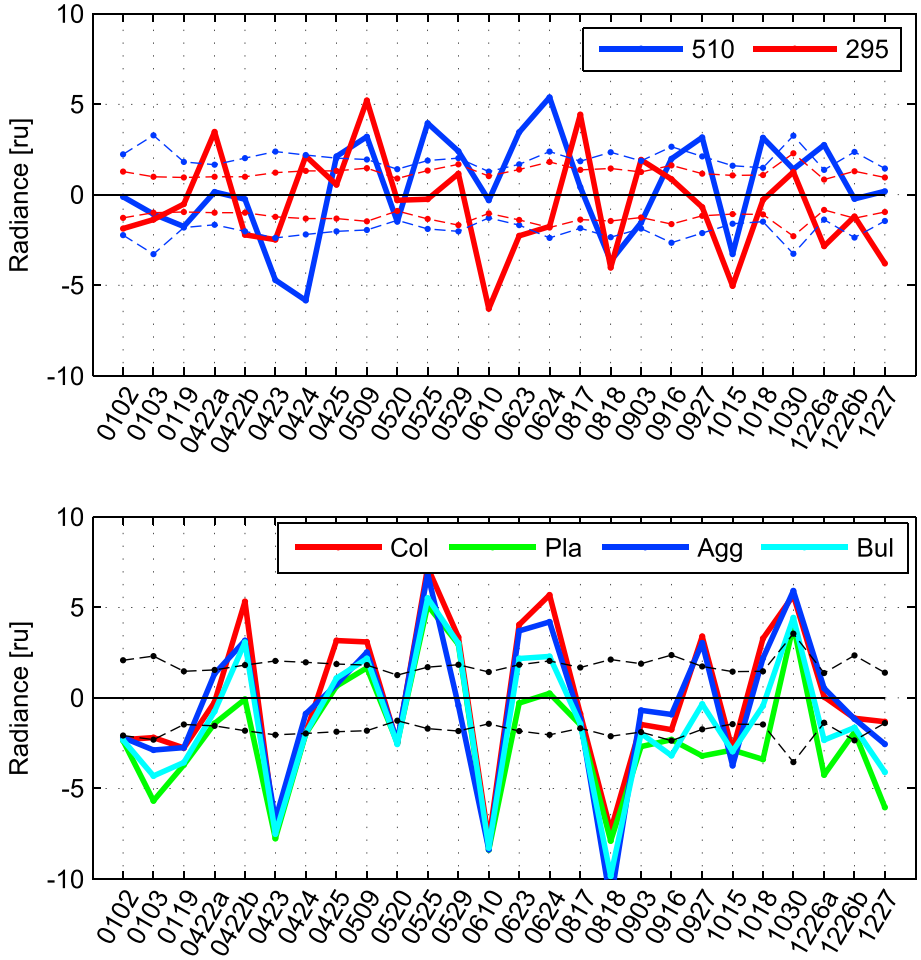

Figure 8. (upper panel) Difference between simulations and measurements in the two selected microwindows (around 510 and 295 cm^{-1}) for aggregates. (lower panel) Difference between simulations and measurements in the microwindows around 410.4 cm^{-1} for different crystal shapes. Results are plotted versus measurement time and mean measurement errors in each microwindows are shown as dashed lines.

noise level. This makes the retrieval very difficult to be performed and somehow dependent on the choice of the channels used in the procedure. In our retrieval process, we have selected 22 channels, which imply a considerable effort in terms of computational power and time because of the full scattering computations. Channels have been selected in order to catch the spectral variations of the cloud radiative properties (in accordance with ice refractive indexes, crystals size, and habit) in the main window.

The residuals in the FIR are evaluated for a selected number of (so called) "dirty" windows. Figure 8 (upper panel) shows the residuals versus time computed for the aggregate habit in two m-ws centered at 295 and 510 cm^{-1}. The selected windows are, respectively, representatives of a moderate high and a moderate low absorption of ice in the FIR band. In both channels, residuals computed in clear conditions (Rizzi et al., 2016) show a slightly negative bias (not shown here). At 295 cm^{-1}, the residuals show a large variability, and the average is close to zero; no trend is observed in the plot for increasing COD. At 510 cm^{-1}, the residuals are mostly positive and increase for increasing COD, for any of the assumed crystal habits, with only slight differences in the absolute values.

In the lower panel of Figure 8, the residuals in the m-w centered at 410.4 cm^{-1} are plotted as a function of time for all the crystal habits. The imaginary part of the refractive index of ice is particularly low at around these wave numbers (the lowest value in the REFIR-PAD measurement spectral range is found at 434 cm^{-1}). For this reason, the absorption and emission processes by the cloud particles are minimized, and scattering effects (related to crystals' shape) are expected to be observed in the simulated spectrum (Yang et al., 2003). The sensitivity of the radiance to the crystals' shape is highlighted by differences in the residuals that

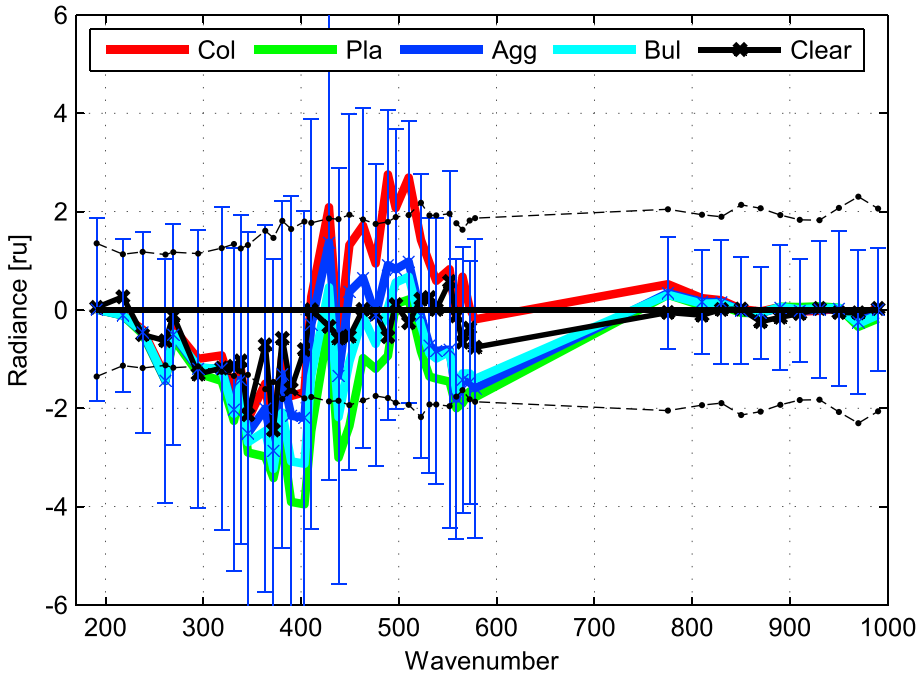

Figure 9. Spectral residuals averaged over all 26 cases, for the four crystal habits. Vertical bars are one standard deviation for the aggregates habit only. Dashed lines denote the average measurement errors. Average residuals for the clear sky cases presented in Rizzi et al. (2016) are also plotted for comparison.

can be as high as 5 r.u. at 410.4 cm^{-1} among the various crystal shapes. The two extremes are obtained in case of plates and solid columns that are, respectively, the most compact and thinnest shape among the considered ones.

In Figure 9, the average spectral structure of the residuals in FIR m-ws and in the main IR window is shown for each crystal habit. The average is computed over all the 26 case studies. Vertical bars corresponding to $1 - \sigma$ deviation from the aggregate mean are also plotted in the figure, and their amplitudes suggest a considerable spread among the cloudy cases. The variability is larger for wave numbers between 350 and 450 cm^{-1} where the more transparent m-ws are placed and where the scattering behavior due to the crystal shape affects more the simulations. For all the shapes, the spectral pattern is characterized by a mean underestimation in the 300–400 cm^{-1} interval and a small overestimation at around 500 cm^{-1}. Plates show the largest mean residuals at around the 410 cm^{-1}, where the pure ice has a minimum in the absorption properties, while columns show the worst results at around 500 cm^{-1} where the ice absorption is moderate. The spectral variability of the mean residual for cloudy scenes has a spectral pattern that is very similar (in particular for bullet rosettes and aggregates) to the yearly mean residual in clear conditions, also plotted in Figure 9 as a black line.

The results reported in Figure 9 are linked to the modeling of the atmospheric state (i.e., the Precipitable Water Vapor [PWV] and temperature profile) and cloud features (i.e., COD, cloud r_{eff}, PSD, and particle habit) since all these parameters affect the downwelling radiance with nonlinear effects. Rizzi et al. (2016) found that clear sky residuals were mainly due to the representation and modeling of water vapor. Under the hypothesis that the retrieved cloud parameters and their simulated cloud properties are representative of the observed scene, we would expect that mean residuals in cloudy conditions were about the same as for the clear data set. However between 450 and 550 cm^{-1}, the clear-sky mean residuals are generally smaller than the cloudy ones. At these wave numbers, in presence of a cloud, the sensitivity to the assumed crystal habit is the largest, as can be seen by the spread of the residuals for different habits.

In order to evaluate the role of COD and PWV on the residuals in the FIR and their possible spectral structure, data are divided in subsets. The total set composed of 26 cloud cases is separated into four groups depending on relatively large or small values of COD and PWV (the thresholds are 0.5 mm for PWV and 0.6 for COD). Results are shown in Figure 10 for the aggregates habit assumption (red line) together with

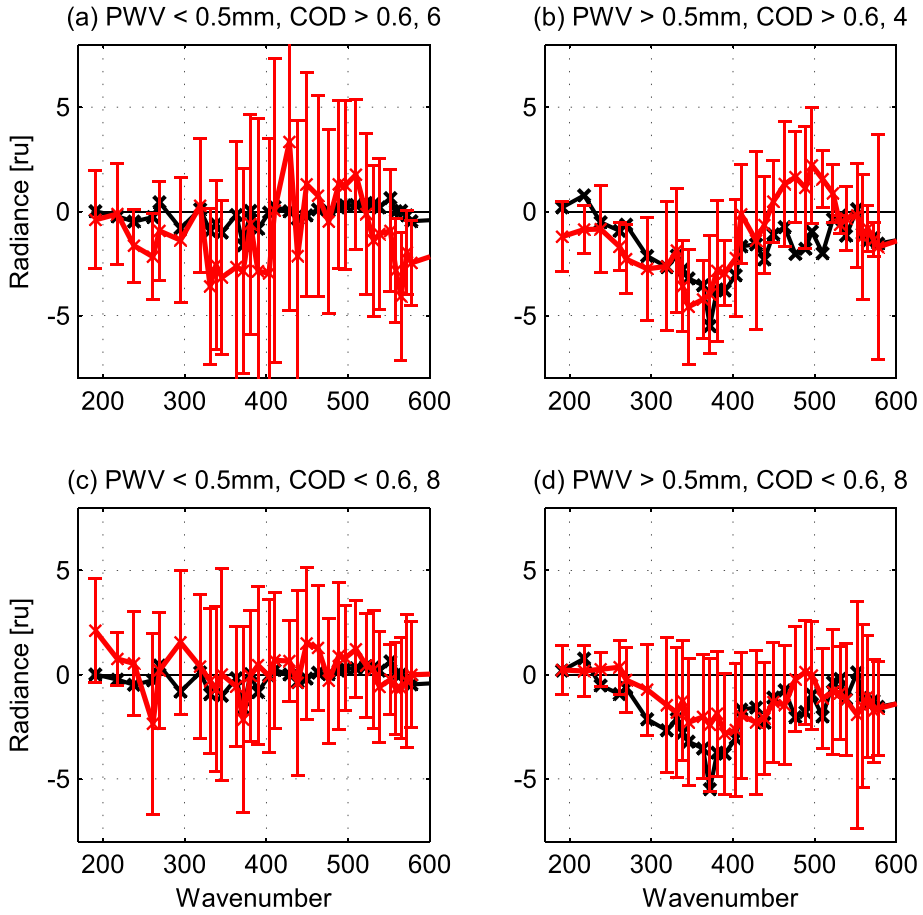

Figure 10. Simulations-measurements residuals for four groups of data depending on COD (larger than 0.6 for panels (a) and (b) and lower than 0.6 for panels (c) and (d)) and PWV (smaller than 0.5 mm on the left column and above on the right one) in the selected Far InfraRed microwindows. Black curves show the residuals for clear sky for the same PWV content range during the same year of measurement, 2013. PWV = Precipitable Water Vapor; COD = Cloud Optical Depth.

results obtained for clear data set and falling in the same PWV conditions. For the cases for which the COD falls in the smaller range (bottom panels), the residuals are the closest to the clear case results, that, for very low values of PWV (left bottom panel), are close to zero in all the FIR. For larger COD (upper panels of Figure 10), the cloud signal has a larger impact on the results, and some differences in the residuals with respect to the clear cases are observed for wave numbers larger than 400 cm^{-1}. At these wave numbers, the spectral structure of the residual depends on the assumed habits (as shown in Figure 9) and retrieved microphysical properties. Also in this case, for very low values of PWV (upper left panel), the results are close to zero. It is seen that residuals below 350 cm^{-1} are very similar to the clear sky cases for all the ranges of the COD. The correlation coefficient between the black and the red curves (respectively, clear and cloudy cases) for wave numbers smaller than 350 cm^{-1} is equal to 0.96 for Figure 10d (small COD and high PWV) and decreases only to 0.54 for Figure 10a (large COD and low PWV).

As noticed, the atmospheric water vapor content has a not-negligible effect on the residuals. In case of thin high clouds, the water vapor is almost totally placed between the sensor and the cloud layers, and thus, its radiative interaction with the cloud (whose signal is small since COD is small) is almost totally limited to an attenuation effect of the weak background radiance. In these cases (that could be represented by the bottom plots of Figure 10), the cloud mean residuals are very similar to the clear ones for similar water vapor contents. Otherwise, in the presence of a low altitude cloud with large COD, the radiative transfer accounts for multiple scattering effects and radiative interactions between water vapor and cloud layers (i.e., cloud base reflection of photons emerging from water vapor layers). For these cases, disentangling water vapor and cloud contribution is more difficult.

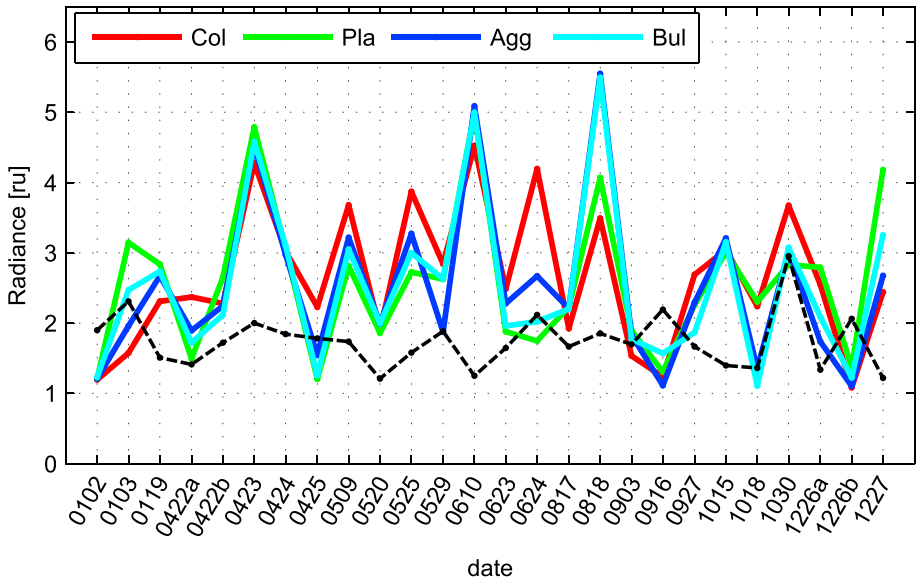

Figure 11. Mean FIR absolute residuals versus time of the year, obtained through an average over selected microwindows. Results are shown for columns, plates, aggregates, and bullet rosettes with REFIR-Prototype for Applications and Development measurement error averaged over all FIR microwindows superimposed in black dashed line. FIR = Far InfraRed.

In Figure 11, absolute differences between simulations and data, averaged over the main FIR windows channels (all m-ws from 380.8 to 580.0 cm^{-1}), are plotted for all the habits. The plot also reports the $2-\sigma$ REFIR-PAD errors (for details on the error analysis, see Rizzi et al., 2016) to provide an idea of the extent of the residuals in comparison with total measurement uncertainties. In about one third of the analyzed cases, the total FIR residuals show very similar values independently of the selected habits: This happens in particular, in correspondence of observational conditions for which the cloud has a small OD (see back to Figure 5). On the contrary, cloud cases characterized by large COD (e.g., those observed in June 2013) show the largest spread in the results, and for some observations, the performed analysis suggests the inadequacy of specific shapes among the assumed ones. For some cases, that is, 22 April, 29 May, and 27 September 2013, an indication of a preferred habit assumption is derived thus providing a first retrieval of the cloud crystals shape from IR data (respectively, plates, aggregates, and bullet rosettes).

6. Summary

An analysis is performed on FIR and mid-IR downwelling spectral radiance collected by the FTS REFIR-PAD based at Dome-C Concordia station on the Antarctic Plateau from December 2012 to December 2013. First, a SVM cloud identification and classification algorithm is applied to the whole data sets, and cloud occurrence statistics are provided. About 45% of the collected radiance spectra resulted clear; about 36% cloudy and the rest were not classified. A cloud subclassification is also performed showing that the majority of the clouds were precipitating clouds. Nonprecipitating ice clouds are detected in the 20% and liquid water clouds in the 10% of the overall cloud cases. The large fraction of the unclassified spectra makes the cloud occurrence statistic still uncertain. The SVM algorithm is also used to highlight the information content of the FIR part of the spectrum. The code makes use of spectral features (that in our case are BT differences) to classify cloudy spectra; it is shown that within the most important six features used to classify liquid phase from ice clouds, five features involve FIR channels. The same holds also in distinguish precipitating from not-precipitating clouds. Among the not-precipitating ice clouds observations, 26 cases are selected for their time proximity with radiosonde launch and contemporaneity with LIDAR measurements. Sondes and LIDAR ancillary data allowed characterization of temperature and water vapor profiles and definition of cloud geometrical properties. Retrievals of COD and effective dimensions are performed using data in the main IR channel and for different habit assumptions. Derived optical depths range between 0.1 and 1.3 and show a temperature dependence: average optical depth values of 0.38 for temperature less than 230 K and 0.59 for higher temperatures. The retrieved effective radius span from 2 to 120 μm with averagely smaller

values (19 μm) for cold clouds (T less than 23 K) and larger ones (35 μm) for warm clouds. Numerical values reported in parentheses are for the aggregates habit hypothesis. Based on the retrieval results, forward simulations all over the REFIR-PAD spectral range are performed for the multiple habits assumptions. The largest sensitivity to crystal shape is found in the 400- to 550-μm interval. Residuals in the middle and far IR windows are evaluated for selected window channels. It is observed that the spectral structure of the residuals in presence of clouds resembles the pattern obtained when clear sky simulations are accounted for (for the same yearly observational data set). The role of COD and PWV is studied by analyzing the residuals for subsets with large or small COD and PWV values. It is shown that the smallest residuals are found for the smallest PWVs. For larger PWVs, high correlation values are found for the clear and cloudy sky residuals suggesting a not-negligible role of water vapor modeling. Finally, the comparison of the residuals for multiple habit assumptions does not allow a clear identification of the cloud crystal shape in the most of the cases analyzed except for few cases for which the overall residuals are within two standard deviations only for one specific shape and not for the others. These cases represent the firsts tentatives habits retrievals from FIR spectral data.

The study performed in this paper using ground-based measurements is preparatory for new space-borne sensors using the FIR portion of the emitted spectrum. As shown in the paper, the FIR spectral region allows to improve the quality of the retrieval of cirrus properties, which critically influence the ERB and climate sensitivity. To date, there have been very few spectral observations of cirrus clouds spanning the FIR, precluding a rigorous test of how well these models are able to capture the radiative signature of cirrus within this spectral region. Recently two missions that are under study, FORUM by ESA and Polar Radiant Energy in the Far-InfraRed Experiment by NASA, can reverse this situation, and the study presented in this paper can be useful to exploit the new coming FIR measurements.

Acknowledgments
The present work is in preparation of the FORUM mission, which has recently been selected by the European Space Agency (ESA) as one of the two candidates for the Earth Explorer 9 mission programme. The mission will undergo the industrial and scientific Phase-A study in 2018–2019. FORUM related studies are supported by projects of the Italian Space Agency, ASI, SCIEF project, and of the ESA. Data are available online (http://refir.ino.cnr.it/refir-pad-domeC). Data and information on radiosounding measurements were obtained from IPEV/PNRA Project "Routine Meteorological Observation at Station Concordia (www.climantartide.it).

References

Bailey, M. P., & Hallett, J. (2009). A comprehensive habit diagram for atmospheric ice crystals: Confirmation from the laboratory, AIRS II, and other field studies. *Journal of the Atmospheric Sciences*, *66*(9), 2888–2899.

Bhawar, R., Bianchini, G., Bozzo, A., Cacciani, M., Calvello, M., Carlotti, M., et al. (2008). Spectrally resolved observations of atmospheric emitted radiance in the H_2O rotation band. *Geophysical Research Letters*, *35*, L04812. https://doi.org/10.1029/2007GL032207

Bianchini, G., Di Natale, G., Del Guasta, M., & Palchetti, L. (2016). Two years of spectrally-resolved measurements of the Antarctic downwelling atmospheric radiance within the COMPASS project. Fourier Transform Spectroscopy, pp. FTu3C–3, Optical Society of America.

Bianchini, G., Palchetti, L., & Carli, B. (2006). A wide-band nadir-sounding spectroradiometer for the characterization of the Earth's outgoing long-wave radiation. Remote Sensing, p. 63610A, International Society for Optics and Photonics.

Bianchini, G., Palchetti, L., Guasta, M. D., & Natale, G. D. (2013). The PRANA experiment: Characterization of atmospheric downwelling long-wavelength radiance over the Antarctic plateau. In *EGU General Assembly Conference Abstracts, EGU General Assembly Conference Abstracts* (Vol. *15*, pp. 14033).

Bozzo, A., Maestri, T., & Rizzi, R. (2010). Combining visible and infrared radiometry and lidar data to test simulations in clear and ice cloud conditions. *Atmospheric Chemistry and Physics*, *10*(15), 7369–7387.

Bozzo, A., Maestri, T., Rizzi, R., & Tosi, E. (2008). Parameterization of single scattering properties of mid-latitude cirrus clouds for fast radiative transfer models using particle mixtures. *Geophysical Research Letters*, *35*, L16809. https://doi.org/10.1029/2008GL034695

Cox, C., Harries, J., Taylor, J., Green, P., Baran, A., Pickering, J., et al. (2010). Measurement and simulation of mid- and far-infrared spectra in the presence of cirrus. *Quarterly Journal of the Royal Meteorological Society*, *136*(648), 718–739.

Di Giuseppe, F., & Rizzi, R. (1999). Far infrared scattering effects in cloudy sky, physics and chemistry of the Earth, part B: Hydrology. *Oceans and Atmosphere*, *24*, 191–202.

Di Natale, G., Palchetti, L., Bianchini, G., & Guasta, M. D. (2017). Simultaneous retrieval of water vapour, temperature and cirrus clouds properties from measurements of far infrared spectral radiance over the Antarctic plateau. *Atmospheric Measurement Techniques*, *10*(3), 825–837.

Evans, K., & Stephens, G. (1991). A new polarized atmospheric radiative transfer model. *Journal of Quantitative Spectroscopy and Radiative Transfer*, *46*(5), 413–423.

Foot, J. (1988). Some observations of the optical properties of clouds. II: Cirrus. *Quarterly Journal of the Royal Meteorological Society*, *114*(479), 145–164.

Grenfell, T., & Warren, S. (2010). Representation of a nonspherical ice particle by a collection of independent spheres for scattering and absorption of radiation. *Journal of Geophysical Research*, *104*, 697–709. https://doi.org/10.1029/1999JD900496

Ham, S.-H., Sohn, B.-J., & Baum, B. (2009). Assessment of the quality of MODIS cloud products from radiance simulations. *Journal of Applied Meteorology and Climatology*, *48*, 1591–1612.

Hansen, J., & Travis, L. (1974). Light scattering in planetary atmospheres. *Space Science Reviews*, *16*(4), 527–610.

Harries, J., Carli, B., Rizzi, R., Serio, C., Mlynczak, M., Palchetti, L., et al. (2008). The far infrared Earth. *Reviews of Geophysics*, *46*, RG4004. https://doi.org/10.1029/2007RG000233

Hogan, A. W. (1975). Summer ice crystal precipitation at the South Pole. *Journal of Applied Meteorology*, *14*(2), 246–249.

Huang, X., Chen, X., Zhou, D. K., & Liu, X. (2016). An observationally based global band-by-band surface emissivity dataset for climate and weather simulations. *Journal of the Atmospheric Sciences*, *73*(9), 3541–3555.

Lachlan-Cope, T. (2010). Antartic clouds. *Polar Research*, *29*, 150–158.

Lachlan-Cope, T., Ladkin, R., Turner, J., & Davison, P. (2001). Observations of cloud and precipitation particles on the Avery Plateau. *Antartic Science*, *13*, 339–348.

Lawson, R., Baker, B., Zmarzly, P., O'Connor, D., Mo, Q., Gayet, J., & Shcherbakov, V. (2006). Microphysical and optical properties of atmospheric ice crystals at South Pole Station. *Journal of Applied Meteorology and Climatology*, *45*, 1505–1524.

Liou, K.-N., & Yang, P. (2016). *Light scattering by ice crystals: Fundamentals and applications*. Cambridge, UK: Cambridge University Press.

Liuzzi, G., Masiello, G., Serio, C., Palchetti, L., & Bianchini, G. (2014). Validation of H_2O continuum absorption models in the wave number range 180–600 cm^{-1} with atmospheric emitted spectral radiance measured at the Antarctica Dome-C site. *Optics Express*, *22*(4), 16784–16801.

Lubin, D., & Harper, D. (1996). Cloud radiative properties over th South Pole from AVHRR infrared data. *Journal of Climate*, *9*, 3405–3418.

Maestri, T., Di Girolamo, P., Summa, D., & Rizzi, R. (2010). Clear and cloudy sky investigations using Raman lidar and airborne interferometric measures from the European AQUA Thermodynamic Experiment. *Atmospheric Research*, *97*(1-2), 157–169.

Maestri, T., & Holtz, R. E. (2009). Retrieval of cloud optical properties from multiple infrared hyperspectral measurements: A methodology based on a line-by-line multiple-scattering code. *IEEE Transactions on geoscience and remote sensing*, *47*, 2413–2426.

Maestri, T., Rizzi, R., Tosi, E., Veglio, P., Palchetti, L., Bianchini, G., et al. (2014). Analysis of cirrus cloud spectral signatures in the Far InfraRed. *Journal of Quantitative Spectroscopy and Radiative Transfer*, *141*, 49–64.

Mahesh, A., Walden, V. P., & Warren, S. (2001). Ground-based remote sensing of cloud properties over the Antarctic Plateau. Part II: Cloud optical depths and particle sizes. *Journal of Applied Meteorology*, *40*, 1279–1294.

Melgani, F., & Bruzzone, L. (2004). Classification of hyperspectral remote sensing images with support vector machines. *IEEE Transactions on geoscience and remote sensing*, *42*(8), 1778–1790.

Naud, C., Russell, J. E., & Harries, J. E. (2001). Remote sensing of cirrus properties in the far infrared. Europto Remote Sensing (pp. 30–38). International Society for Optics and Photonics.

Pal, S. R., Steinbrecht, W., & Carswell, A. I. (1992). Automated method for lidar determination of cloud-base height and vertical extent. *Applied optics*, *31*(10), 1488–1494.

Palchetti, L., Bianchini, G., Del Guasta, M., & Baglioni, A. (2012). Spectral measurements of the atmospheric thermal infrared emission in Antarctica. AGU Fall Meeting Abstracts.

Palchetti, L., Bianchini, G., Di Natale, G., & Del Guasta, M. (2015). Far-infrared radiative properties of water vapor and clouds in Antarctica. *Bulletin of the American Meteorological Society*, *96*(9), 1505–1518.

Ricaud, P., Bazile, E., del Guasta, M., Lanconelli, C., Grigioni, P., & Mahjoub, A. (2017). Genesis of diamond dust, ice fog and thick cloud episodes observed and modelled above Dome C, Antarctica. *Atmospheric Chemistry & Physics*, *17*(8), 5221–5237.

Rizzi, R., Arosio, C., Maestri, T., Palchetti, L., Bianchini, G., & Del Guasta, M. (2016). One year of downwelling spectral radiance measurements from 100 to 1400 cm^{-1} at Dome Concordia: Results in clear conditions. *Journal of Geophysical Research: Atmospheres*, *121*, 10–937. https://doi.org/10.1002/2016JD025341

Rizzi, R., Maestri, T., & Bozzo, A. (2007). Reference tool for simulation of VIS/NIR spectral radiances. Eumetsat Report, contract EUM/CO/06/1529/PS 116.

Shimizu, H. (1963). Long prism crystals observed in the precipitation in Antarctica. *Journal of the Meteorological Society of Japan*, *41*, 305–307.

Stone, R. (1993). Properties of Austral winter clouds derived from radiometric profiles at the South Pole. *Journal of Geophysical Research*, *12*, 961–971.

Swartz, W. H., Lorentz, S. R., Huang, P. M., Smith, A. W., Deglau, D. M., Liang, S. X., et al. (2016). The Radiometer Assessment using Vertically Aligned Nanotubes (RAVAN) cubesat mission: A pathfinder for a new measurement of Earth's radiation budget.

Theodoridis, S., Pikrakis, A., Koutroumbas, K., & Cavouras, D. (2010). *An introduction to pattern recognition*. A MATLAB Approach: Academic Press.

Veglio, P., & Maestri, T. (2011). Statistics of vertical backscatter profiles of cirrus clouds. *Atmospheric Chemistry and Physics*, *11*, 12925–12943.

Walden, V., Warren, S., & Tuttle, E. (2003). Atmospheric ice crystals over the Antarctic Plateau in winter. *Journal of Applied Meteorology*, *42*, 1391–1405.

Yang, P., Bi, L., Baum, A., Liou, K.-N., Kattawar, G. W., Mishchenko, M. I., & Cole, B. (2013). Spectrally consistent scattering, absorption and polarization properties of atmospheric ice crystals at wavelengths from 0.2 to 100 μm. *Journal of the atmospheric sciences*, *70*, 330–347.

Yang, P., Mlynczak, M. G., Wei, H., Kratz, D. P., Baum, B. A., Hu, Y. X., et al. (2003). Spectral signature of ice clouds in the far-infrared region: Single-scattering calculations and radiative sensitivity study. *Journal of Geophysical Research*, *108*(D18), 4569. https://doi.org/10.1029/2002JD003291